Simulation of Spatially Resolved Electron Energy Loss Near-Edge Structure for Scanning Transmission Electron Microscopy

M. P. Prange, M. P. Oxley, M. Varela, S. J. Pennycook, and S. T. Pantelides

Phys. Rev. Lett. **109**, 246101 — Published 12 December 2012

DOI: 10.1103/PhysRevLett.109.246101

Simulation of Spatially-Resolved Electron Energy Loss Near-Edge Structure for Scanning Transmission Electron Microscopy

M. P. Prange,[1, 2, *] M. P. Oxley,[1, 2, †] M. Varela,[2] S. J. Pennycook,[2, 1] and S. T. Pantelides[1, 2, 3]
[1]*Department of Physics and Astronomy, Vanderbilt University, Nashville, TN 37235*
[2]*Materials Science and Technology Division, Oak Ridge National Laboratory, Oak Ridge, Tennessee 37831*
[3]*Department of Electrical Engineering and Computer Science, Vanderbilt University, Nashville, TN 37235*

(Dated: November 9, 2012)

Aberration-corrected scanning transmission electron microscopy yields probe-position dependent energy-loss near-edge structure (ELNES) measurements, potentially providing spatial mapping of the underlying electronic states. ELNES calculations, however, typically describe excitations by a plane wave traveling in vacuum, neglecting the interaction of the electron probe with the local electronic environment as it propagates through the specimen. Here we report a methodology that combines a full electronic-structure calculation with propagation of a focused beam in a thin film. The results demonstrate that only a detailed calculation using this approach can provide quantitative agreement with observed variations in probe-position dependent ELNES.

PACS numbers: 68.37.Lp, 79.20.Uv, 68.37.Ma, 61.85.+p

Continuing advances in scanning transmission electron microscopy (STEM), including aberration-correction and enhanced stability, have made possible imaging of thin films, interfaces and individual impurities with sub-Ångström resolution [1–5]. Increased probe currents and post-specimen optics have also enabled atomic-resolution imaging based on core-level electron-energy-loss spectroscopy (EELS). EELS provides both chemical mapping and information about the local atomic arrangements and the corresponding electronic states, which is reflected in the energy-loss near-edge structure (ELNES) [6–10], and allows even the extraction of information about magnetic ordering [11]. Hence, STEM-EELS is a uniquely powerful tool for investigating and understanding the atomic-scale properties of complex inhomogeneous materials.

The extraction of information from EELS, however, requires simulations to relate the strength of the EELS signal to the electronic structure and dynamics of the sample electrons. Since EELS and x-ray absorption spectroscopy (XAS) probe the same electronic excitations, EELS experiments are typically interpreted in terms of calculations originally developed for XAS, assuming that the excitation is caused by a plane wave travelling in vacuum [12–14]. Such approaches, however, do not include any dependence on the probe position, which obviously limits their applicability to STEM-EELS.

On the other hand, the calculation of STEM-EELS images, based on dynamical electron scattering theory and the mixed dynamical form factor (MDFF) [15–17], have typically used isolated atomic models to describe inner-shell ionization [18, 19]. While correctly describing the position and propagation of the incident electron probe through the specimen, this approach fails to incorporate solid-state effects that give rise to ELNES. Hence, such simulations are usually limited to comparisons with experimental chemical maps in which the signal from a given species is integrated over an energy range[6, 7, 10, 11]. Most previous formulations combining density functional calculations with dynamical scattering theory, most notably by Schattschneider and coworkers [20–22], have described plane-wave illumination. An earlier application to STEM-EELS has used a dipole approximation to investigate the intermixing of O K-shell spectra in $SrTiO_3$ [23].

In this Letter, we present a method to calculate STEM-EELS that treats both the fine structure induced by the solid-state environment and the position and dynamical scattering of the probe electrons on the same footing with accurate, detailed theories. The propagation of the incident electron wave function through the specimen is calculated using a Bloch-wave method, which is appropriate for thin specimens [15]. For the electronic excitation by the electron beam, we used density functional theory (DFT) calculations of the available final electronic states in the presence of a core hole, performed within the projector-augmented wave (PAW) method [25]. Since non-dipole allowed transitions have been shown to be important in both electron microscopy [26, 27] and X-ray spectra calculations [28], we compute matrix elements of the operator $e^{i\mathbf{Q}\cdot\mathbf{r}}$ for momentum transfers $\mathbf{Q}$ using the PAW wave functions obtained from the VASP code [29], without invoking the dipole approximation. Initial core states are obtained using the FEFF code [30]. Subsequently, these matrix elements are used to construct the MDFF which, along with the elastic wave function of the probe electron, give the energy-loss spectrum image, including all quantum interference effects.

To illustrate the importance of this work we study the evolution of the O K-shell ELNES in $LaMnO_3$ (LMO) as a a function of STEM probe position. Previous work has revealed variations, with the periodicity of the crystal, in the measured ELNES of both the O K-shell and Mn L_{23} [10]. Such variations are usually associated with changes

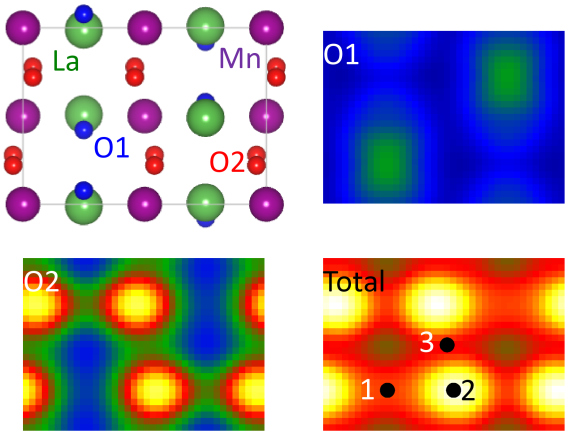

FIG. 1: (color online) Projected structure of LMO in the [010] zone axis orientation and integrated intensities for O1, O2 and the total O signal as a function of probe position. The positions 1, 2 and 3 indicate probe positions used in Fig. 3 below.

in the oxidation state of Mn, which in the LMO case is constant. Due to a Jahn-Teller distortion, however, LMO contains two inequivalent O sites which make distinct contributions to the ELNES. It was suggested that the ELNES variation may be due to a mixing of these two spectra. In this work we show that the variation can only be explained using a full synergy of DFT and dynamical scattering theory, and not by any simple linear combination of spectra calculated using conventional approaches.

The inelastic STEM image for a crystal of thickness t, and for a transition $i \rightarrow f$ may be written [15]

$$\sigma^{i,f}(\mathbf{R},t) = \int_0^t \sum_{\mathbf{h},\mathbf{g}} \Psi^*_{\mathbf{h}}(\mathbf{R},z)\Psi_{\mathbf{g}}(\mathbf{R},z)\mu^{i,f}_{\mathbf{h},\mathbf{g}} dz. \qquad (1)$$

The Fourier space representation of the elastically scattered incident electron, $\Psi_{\mathbf{g}}$, depends on probe position $\mathbf{R}$ and the depth within the crystal z. The vectors $\mathbf{g},\mathbf{h}$ are reciprocal lattice vectors associated with the supercell on which the calculation is performed. In this work we have used a Bloch-wave method which excludes the possibility of ionization caused by the thermally scattered electrons, but the method is easily adapted to include this contribution [24]. The inelastic scattering coefficient for the excitation of a core shell electron $\mu^{i,f}_{\mathbf{h},\mathbf{g}}$ is given by [31],

$$\mu^{i,f}_{\mathbf{h},\mathbf{g}} = \frac{1}{2\pi k V_c}\sum_{\beta} e^{-M_\beta(\mathbf{g}-\mathbf{h})} e^{2\pi i(\mathbf{h}-\mathbf{g})\cdot\boldsymbol{\tau}_\beta} \times \frac{1}{2\pi^2 a_0^2}\int_{\text{det.}} k' \frac{S^{i,f}(\mathbf{Q_h},\mathbf{Q_g})}{|\mathbf{Q_h}|^2|\mathbf{Q_g}|^2} d\Omega_{k'}. \qquad (2)$$

Here $k \equiv |\mathbf{k}|$ is the magnitude of the wave vector of the incident electron $\mathbf{k}$ and V_c is the volume of the crystallographic unit cell. The sum occurs over equivalent atom types β with Debye-Waller factors M_β where $\boldsymbol{\tau}_\beta$ is the position of these atoms within the unit cell. The relativistically corrected Bohr radius is a_0. For a fixed energy, the integration over the scattered electron's wave vector $d\Omega_{k'}$ where $k' \equiv |\mathbf{k}'|$ is limited by the detector. The quantity $\mathbf{Q_g} \equiv \mathbf{q}+\mathbf{g}$ where $h\mathbf{q} = h(\mathbf{k}-\mathbf{k}')$ is the momentum transfer to the crystal.

The MDFF is usually defined with a summation over all initial and final states, including the atomic positions defined in Eq. (2). For consistency with previous STEM imaging simulation notations, we define a MDFF specific to a single transition,

$$S^{i,f}(\mathbf{Q_h},\mathbf{Q_g}) = \langle f|e^{2\pi i\mathbf{Q_h}\cdot\mathbf{r}}|i\rangle\langle i|e^{-2\pi i\mathbf{Q_g}\cdot\mathbf{r}}|f\rangle. \qquad (3)$$

A special case of this expression is $\mathbf{g} = \mathbf{h}$ which is the dynamical form factor (DFF). In particular, the term with $\mathbf{g} = \mathbf{h} = 0$ is corresponds to conventional DFT spectrum calculations.

Matrix elements were calculated for transition energies up to 20 eV beyond the edge onset. A total of 13,000 allowed transitions are in this energy range. Full probe-position-dependant spectra are constructed by convolving the images calculated using Eq. (1) along the energy axis with a 1 eV Gaussian to account for experimental broadening. All image simulations are for 60 keV incident electrons and a probe forming aperture semi-angle of 30 mrad. All simulations include temporal incoherence due to an energy spread of 0.35 eV and a chromatic aberration coefficient of $C_c = 1.3$ mm. A Gaussian source size with a full width half maximum of 0.85 Å is applied to all images. A specimen thickness of 100 Å and a detector semi-angle of 32 mrad are assumed.

In Fig. 1 we show the projected structure of LMO down the [010] zone axis orientation (⟨110⟩ in pseudocubic notation). The positions of columns containing oxygen atom types O1 and O2 are indicated. The simulated intensity, integrated over a 20 eV energy window above the O K-shell edge onset, is shown for core-shell ionization of both the O1 and O2 atoms as well as the total O K-shell signal. The majority of the O signal originates from the O2 sites, due partly to the fact that there are twice as many O2 atoms as O1 atoms. In addition, absorption due to the heavy La columns decreases the O1 signal significantly and the maximum O1 signal is seen between the columns.

In Fig. 2 we show the integrated experimental O K-shell intensity and a typical spectrum. As with the simulation, the bright peaks represent the O2 columns and the O1 positions occur at the minima. All images were acquired on a Nion UltraSTEM operating at 60 kV, with parameters as specified in the theoretical discussion. Spectra have undergone principal component analysis and background subtraction. One property of the O K-shell spectrum associated with the oxidation state of Mn in LMO is the energy separation between the pre-

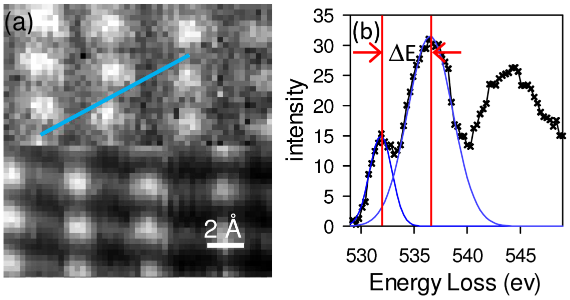

FIG. 2: (color online) (a) Integrated experimental O K-shell intensity (top) and simultaneously acquired ADF signal (bottom). (b) A typical spectrum showing schematically the ΔE measurement. The line scan indicated on (a) is the same as used in Fig. 4

peak and the first main peak, signified ΔE. This separation is determined by fitting two Gaussians to these features, as illustrated schematically in Fig. 2(b). For the experimental spectra these Gaussians are fitted over 5 eV regions of interest (ROI) chosen such that the leading edges of these two features are well described [10]. In this letter we investigate the origins of the observed periodic variation in this quantity.

In Fig. 3 we show simulated spectra as a function of probe position for each O type individually and the total signal. In order to explore the possibility that the ELNES variation is due to a simple mixing of two inequivalent spectra, as discussed above, we also show spectra calculated by weighting $\mu^{i,f}_{\mathbf{0},\mathbf{0}}$ by the appropriate integrated intensities shown in Fig. 1 to produce position dependent spectra, which we dub the WDFF model. The WDFF spectra are shown by the dashed lines. It should be noted that since $\mu^{i,f}_{\mathbf{0},\mathbf{0}}$ contains no spatial information, the WDFF spectra for O1 and O2 do not change shape as a function of probe position, but merely vary in intensity.

For the O1 spectra, there is clear variation in the two features in the first main peak at approximately 534 and 536 eV. For position 1 (between the O1 atoms) the feature at 534 eV is slightly larger than that at 536 eV. This is reversed for the other two probe positions. Above the O2 columns (position 2), the WDFF and the full calculation agree very closely for the O2 signal. Since the total signal is dominated by the O2 signal at this position there is also close agreement between the WDFF and full simulation for the total signal. Away from position 2 the difference between the the WDFF and full simulations is more marked, especially for the total signal where the O1 contribution is significant. While these variations are small, they affect the center of mass of the main peak and hence the measured value of ΔE.

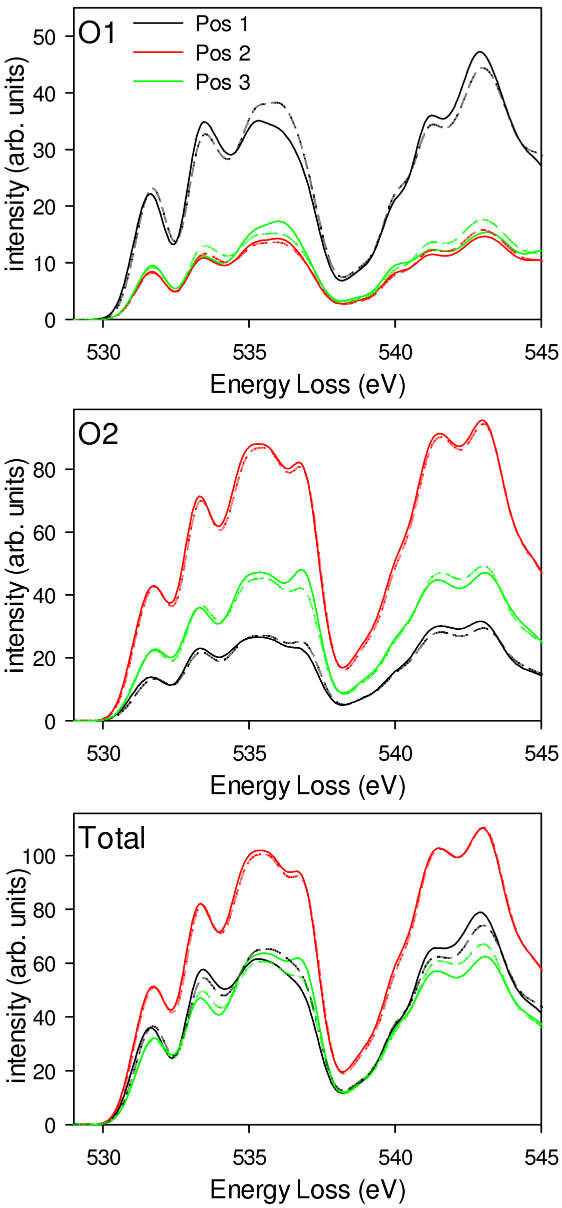

FIG. 3: (color online) Spectra as a function of probe position for O1, O2 and the total signal. The three positions Pos 1 (black), Pos 2 (red) and Pos 3 (green) are shown in Fig. 1. Dashed lines represent the WDFF spectra.

There are a number of differences between the experimental and theoretical spectra, most obviously, the initial feature at 534 eV in the first main peak of the theoretical spectra is not present in the experimental results. This may be due to a number of factors, for example there are many LMO structures of differing stoichiometry in the literature [32–35] and the theoretical spectrum lacks higher-level corrections beyond the local density approximations for exchange and correlation. It is however not the goal of this work to perfectly match the shape of the spectra, but instead to understand the origin of the variations in ELNES as a function of probe position. The value of ΔE for the theoretical spectra is determined in an identical manner to that of the experiment, except, to exclude the extra feature appearing in the simulations near 534 eV, a reduced ROI of 3 eV is used in fitting the Gaussians. As before, the first ROI is positioned so that the fitted Gaussian matches the leading edge of the prepeak. The second ROI is positioned to provide the best match to the leading edge of the feature centered just above 535 eV.

In Fig. 4 we compare the experimental 2D plot of ΔE with both the full calculation and the WDFF. While noisy, the experiment varies over a range of 0.1-0.2 eV along the line scan. This is well matched by the full simulation. The WDFF result shows only a small out-of-phase variation along the same line scan. Even with the line scan shifted to illustrate the full dynamic rage of Fig. 4 (e), the value of ΔE varies only by approximately 0.06 eV. The weighted addition of DDFs is clearly not sufficient to explain the observed variations. In addition, the peaks in the ΔE signal are shifted with respect to the experiment and full simulation which are in phase.

While the WDFF spectrum cannot vary as a function of probe position for each atom type O1 and O2, The full calculation does not have this limitation. Shown in Fig. 5 is the variation in ΔE for each O type. The variation is slightly larger than that of the total signal. This implies that the variation of ΔE is not simply due to the linear combination of two different spectra; indeed the effect of the summation is to slightly damp this variation.

We have shown that the evolution of ELNES as a function of STEM probe position can only be fully explained using a detailed combination of DFT and dynamical scattering theory via the MDFF. In other words, the spectra observed by atomic resolution STEM are a function not only of the local electronic environment, but also a product of the experimental conditions. It is therefore not possible to do quantitative analysis of STEM EELS experiments based on DFT alone. These simulations are an essential part of the interpretation of more complex materials systems such as defects, thin films, interfaces and ordered vacancies.

We would like to thank L.J. Allen for useful discussions and D. Mandrus and R. Jin for providing the LMO powders. This work was supported in part by DOE grant no. DE-FG02-09R46554 (MPP, MPO, STP), by the DOE Office of Basic Energy Sciences, Materials Sciences and Engineering Division (SJP,MV,STP) and by the McMinn Endowment at Vanderbilt University (STP). Computations were performed at the National Energy Research Scientific Computing Center.

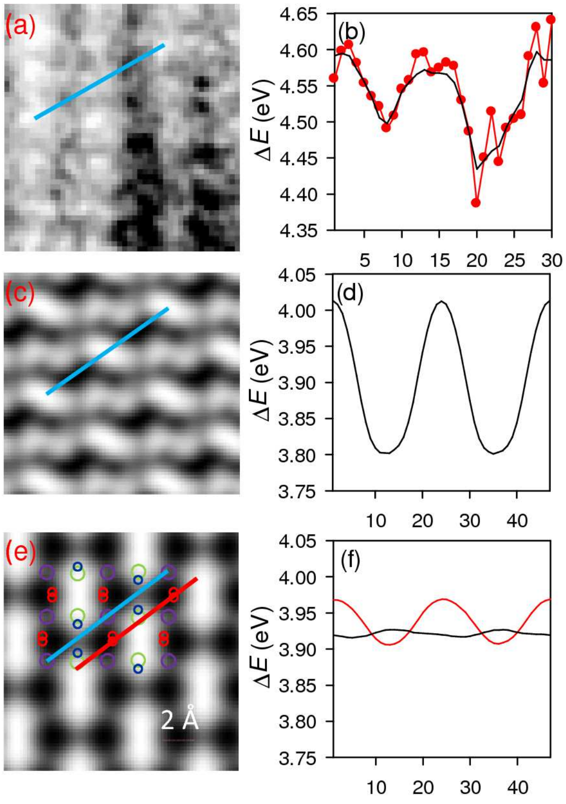

FIG. 4: (color online) Two dimensional plots of ΔE and indicated line scans for experiment (a) & (b), theory (c) & (d), and weighted DFF, (e) & (f). Line scans are taken diagonally across the unit cell shown schematically on (e) except for the red line on (e) & (f), which is shifted to illustrate the maximum contrast observed. The ΔE axis encompasses a range of 0.3 eV in all cases. Different grey scales are used in panels (a), (c) and (e) in order to bring out the full contrast in each case. (a) has been smoothed using the Digital Micrograph smooth function with the default low-pass 3×3 light setting. The line scan of the unsmoothed ΔE is shown by the red line/circles.

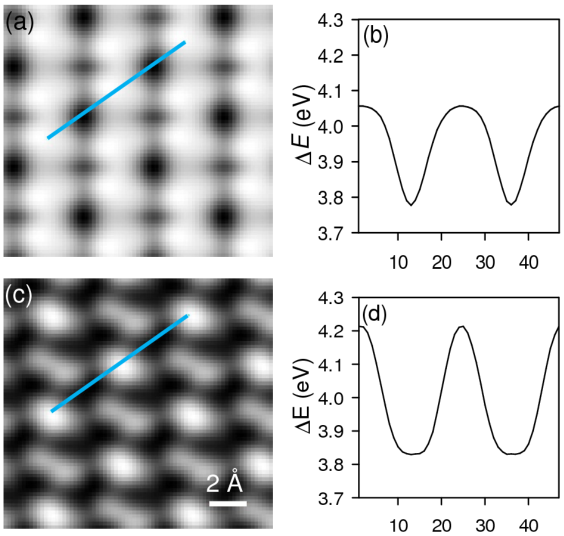

FIG. 5: (color online) Two dimensional plots of ΔE and indicated line scans for O1 (a) & (b), and O2 (c) & (d).

---

[*] Present address Fundamental and Computational Sciences Directorate, Pacific Northwest National Laboratory, Richland, WA 99354

[†] Corresponding Author `oxleymp@ornl.gov`

[1] P. E. Batson, N. Dellby, and O. L. Krivanek, Nature **418**, 617 (2002).
[2] P. D. Nellist *et al.*, Science **305**, 1741 (2004).
[3] H. Sawada *et al.*, Japanese Journal of Applied Physics **46**, L568 (2007).
[4] A. R. Lupini *et al.*, Microscopy and Microanalysis **15**, 441 (2009).
[5] R. Erni, M. D. Rossell, C. Kisielowski, and U. Dahmen, Phys. Rev. Lett. **102**, 096101 (2009).
[6] M. P. Oxley *et al.*, Phys. Rev. B **76** (2007).
[7] M. Bosman *et al.*, Phys. Rev. Lett. **99**, 086102 (2007).
[8] K. Kimoto *et al.*, Nature **450**, 702 (2007).
[9] D. A. Muller *et al.*, Science **319**, 1073 (2008).
[10] M. Varela *et al.*, Phys. Rev. B **79**, 085117 (2009).
[11] J. Gazquez *et al.* , Nano Lett. **11**, 973 (2011).
[12] R. Buczko *et al.*, Phys. Rev. Lett. **85**, 2168 (2000).
[13] C. Hébert, Micron **38**, 12 (2007).
[14] K. Jorissen, J. J. Rehr, and J. Verbeeck, Phys. Rev. B **81**, 155108 (2010).
[15] L. J. Allen *et al.*, Ultramicroscopy **96**, 47 (2003).
[16] C. Dwyer, Ultramicroscopy **104**, 141 (2005).
[17] H. Kohl and H. Rose, Advances in Imaging and Electron Physics **65**, 173 (1985).
[18] V. W. Maslen, J. Phys. B **16**, 2065 (1983).
[19] M. P. Oxley and L. J. Allen, Phys. Rev. B **57**, 3273 (1998).
[20] M. Nelhiebel *et al.*, Phys. Rev. B **59**, 12807 (1999).
[21] M. Nelhiebel, P. Schattschneider, and B. Jouffrey, Phys. Rev. Lett. **85**, 1847 (2000).
[22] J. Rusz, S. Rubino, and P. Schattschneider, Phys. Rev. B **75**, 214425 (2007).
[23] C. Witte *et al.*, Phys. Rev. B **80**, 184108 (2009).
[24] S. D. Findlay *et al.*, Ultramicroscopy **104**, 126 (2005).
[25] P. E. Blöchl, Phys. Rev. B **50**, 17953 (1994).
[26] A. J. D'Alfonso *et al.*, Ultramicroscopy **108**, 677 (2008).
[27] S. Löffer *et al.*, Ultramicroscopy **111**, 1163 (2011).
[28] J. A. Soininen, A. L. Ankudinov, and J. J. Rehr, Phys. Rev. B **72**, 045136 (2005).
[29] G. Kresse and J. Furthmüller, Phys. Rev. B **54**, 11169 (1996).
[30] J. J. Rehr *et al.*, C. R. Phys. **10**, 548 (2009).
[31] L. J. Allen and T. W. Josefsson, Phys. Rev. B **52**, 3184 (1995).
[32] P. Norby, E. Krogh Andersen, and N. H. Andersen, J. Solid State Chem. **119**, 191 (1995).
[33] B. C. Hauback, H. Fjellvag, and N. Sakai, J. Solid State Chem. **124**, 43 (1996).
[34] N. Sakai, H. Fjellvag, and B. Lebech, Acta Chem. Scan. **51**, 904 (1997).
[35] J. Rodríguez-Carvajal *et al.*, Phys. Rev. B **57**, R3189 (1998).